Atomic Layer Deposition of MoSe₂ Using New Selenium Precursors

Raul Zazpe[a,b], Jaroslav Charvot[c], Richard Krumpolec[d], Luděk Hromádko[a,b], David Pavliňák[d], Filip Dvorak[a], Petr Knotek[e], Jan Michalicka[b], Jan Přikryl[a], Siowwoon Ng[b], Veronika Jelínková[f], Filip Bureš[c], Jan M. Macak[a,b,*]

[a] Center of Materials and Nanotechnologies, Faculty of Chemical Technology, University of Pardubice, Nam. Cs. Legii 565, 530 02 Pardubice, Czech Republic
[b] Central European Institute of Technology, Brno University of Technology, Purkynova 123, 612 00 Brno, Czech Republic
[c] Institute of Organic Chemistry and Technology, Faculty of Chemical Technology, University of Pardubice, Studentská 573, 532 10 Pardubice, Czech Republic
[d] R & D Center for Low-Cost Plasma and Nanotechnology Surface Modifications, Department of Physical Electronics, Faculty of Science, Masaryk University, Kotlářská 267/2, 611 37 Brno, Czech Republic
[e] Department of General and Inorganic Chemistry, Faculty of Chemical Technology, University of Pardubice, Studentska 573, 532 10 Pardubice, Czech Republic
[f] The Institute of Technology and Business in České Budějovice, Okružní 517/10, 370 01 České Budějovice, Czech Republic

ARTICLE INFO

ABSTRACT

Among the emerging 2D materials, transition metal chalcogenides are particularly encouraging as alternative semiconducting graphene-like nanomaterial. Recently, 2D MoSe₂ has been gaining interest due to its intriguing properties, in many ways exceeding those of the extensively studied MoS₂. The deposition of 2D nanomaterials in a conformal and uniform fashion on complex-shaped nanostructures is highly appealing but only achievable by atomic layer deposition (ALD). Unfortunately, the synthesis of MoSe₂ by ALD is hindered by a current substantial lack of feasible Se precursors. In this work, we synthesized a set of alkysilyl $(R_3Si)_2Se$ and alkylstannyl $(R_3Sn)_2Se$ compounds and studied their suitability as Se ALD precursors. Thus, ALD processes carried out using $MoCl_5$ as Mo precursor counterpart were followed by an extensive characterization of the as deposited material. The corresponding results revealed successful deposition of MoSe₂ nanostructures on substrates of different nature with dominant out-of-plane orientation. Eventually, the growth evolution of the MoSe₂ during the very early ALD stage was studied and described, displaying concomitant in-plane and out-of-plane MoSe₂ growth. All in all, a set of suitable Se precursors presented herein paves the way for the deposition of 2D MoSe₂ with all the own ALD benefits and allow the further study of its promising properties in a wide number of applications.

1. Introduction

The last decade has witnessed the discovery and great success of graphene with outstanding electronic, chemical, optical and physical properties [1]. These unparalleled properties are well-suited for the development of next generation devices for a wide number of applications ranging from nanoelectronics and optoelectronics to catalysis and sensing [2–5]. However, its metallic nature strongly limits graphene application in photovoltaics and logic devices that demand semiconducting properties. This scenario stimulated a strong interest in the synthesis of semiconducting two-dimensional (2D) nanomaterials. Among the 2D family materials, semiconductor transition metal dichalcogenides (TMDs), MX_2 (M = Mo, W; X = S, Se), have emerged in

the last years [6,7]. Semiconductor TMDs have layered structure where the monolayers stack on each other by van der Waals forces. A TMDs monolayer, consisting of a single layer of transition metal atoms sandwiched between two single layers of chalcogen atoms, exhibits direct transition band gap absent in the bulk counterparts, making them a promising candidate for optoelectronics applications [8,9]. In contrary, TMDs bilayers or multilayers exhibit indirect transition band gap. Regardless the number of layers, the inherent high surface to volume ratio of both mono and multilayered TMDs was demonstrated to be an excellent platform for sensing applications including chemical, gas and biosensors, displaying the ability to detect a wide number of compounds with fast response and recovery time [10–12]. Energy storage applications as Li-ion batteries and supercapacitors also benefited from

their layered structure, excellent electrochemical properties and high surface area [13–15]. In addition, their excellent light absorption and catalytic activities, earth abundancy and low material cost, place 2D TMDs as encouraging candidates to replace noble metals for photocatalytic and electrocatalytic applications [16–19]. As yet, important efforts to tailoring their chemical and physical properties in functional devices by elemental doping, surface modification or enhancing the charge carrier separation via heterojunctions have been made. The use of three-dimensional functional scaffolds to improve the separation and charge carrier transfer, and enhance light absorption is particularly promising [20–23].

Although in the last years 2D MoS_2 has received most attention and efforts from the scientific community, 2D $MoSe_2$ is recently gaining interest due to the inherent metallic nature of Se that offers higher electrical conductivity than that of MoS_2, a crucial property for superior performance in electrochemical applications [24]. In addition, several recent works reported $MoSe_2$ as a promising alternative as electrode in Li and Na ion batteries, and supercapacitors due to its wider inter-layer distance (0.65 nm) [25–33]. In parallel, other works have explored the performance of $MoSe_2$ as sensing, photodetector, electrocatalyst and photocatalyst based on its narrow bandgap (1.33–1.72 eV), high resistance to photo-corrosion and electrochemically active unsaturated Se-edges [34–37]. While its lower Gibbs free energy (close to zero) on $MoSe_2$ edges for hydrogen adsorption, along with its more metallic nature, promotes $MoSe_2$ as a solid alternative catalytic material for hydrogen evolution reaction (HER). Nevertheless, $MoSe_2$ suffers from low light absorption efficiency, slow charge transfer of the intrinsic semiconducting 2H-phase $MoSe_2$, and (as any semiconductor) possesses issues with the recombination of the photogenerated electron–hole pairs. Different approaches have been taken to address those drawbacks by coupling $MoSe_2$ with conducting supporting material and/or maximizing the number of exposed active edges through vertically oriented few-layer $MoSe_2$ nanosheets [38–47].

A wide variety of methods have been reported for the synthesis of nanostructured $MoSe_2$, excellently reviewed in a recent work [48]. Among the different synthesis methods, the most extended are hydrothermal [26,27,41,42,44,47,49,29,30,32–37], solvothermal [38,46,50], liquid exfoliation [12,39,43,45,51], chemical vapor deposition [52–56], electrodeposition [31,57,58], hot filament vapor chemical deposition [59,60] and electrochemical atomic layer deposition [61]. As for the phase structure, $MoSe_2$ can adopt semiconducting 2H trigonal or metallic 1 T octahedral symmetries. Although metallic nature would be desirable for its lower charge transfer resistance, the metallic 1 T phase is metastable and easily converted to the stable 2H phase. Therefore, important efforts have focused on developing methods for the synthesis of metallic phase based on exfoliation and solvothermal techniques [62–66]. Nevertheless, all the aforementioned fabrication methods show different drawbacks, making it difficult to control the morphology, composition and the homogeneity of the synthesized $MoSe_2$. Atomic layer deposition (ALD) is a well-established deposition method based on alternating gas-surface self-limited reactions that offers an unparalleled control over the thickness and the

composition of the materials deposited [67]. In parallel, to date it is by far the best choice for depositing materials in a uniform and conformal fashion over complex and large area substrates. However, except for the pioneering work by Pore et al. [68], which introduced alkysilyl compounds of Se and Te as ALD precursors, there is still a significant lack of suitable Se precursors for the deposition of selenide compounds by ALD. Unlike other hydrides, selenium hydride (H_2Se) is not an option as suitable ALD precursor, due to its extremely high toxicity. Thereby, new compounds have to be searched for this purpose. As candidate for ALD precursor, the compound must fulfill some conditions: to be volatile, be thermally stable (not to decompose) in a temperature range (ALD window), and exhibit self-limited reactivity towards the active sites of the surface provided by the co-reactant [69]. The choice of precursors must render direct and complete ligand exchange reaction.

The motivation of this work is driven by a substantial lack of available Se precursors that hinders the synthesis of selenides by ALD. Inspired by the alkysilyl compounds of Se introduced by Pore et al. [68], we recently successfully grew $MoSe_2$ nanosheets on glass substrates by ALD using $(Me_3Si)_2Se$ and $MoCl_5$ [70]. Herein, we synthesized and explored a wider set of alkylsilyl ($R_3Si)_2Se$ and newly alkylstannyl ($R_3Sn)_2Se$ compounds for the growth of $MoSe_2$ nanosheets by ALD using various Mo precursors. We extensively evaluate these Se compounds in combination with different molybdenum precursors, namely molybdenum pentachloride ($MoCl_5$), molybdenum hexacarbonyl [$Mo(CO)_6$] and bis(t-butylimido)-bis(dimethylamino) molybdenum [$Mo(NMe_2)_2(NtBu)_2$] as reliable Se precursors candidates. The morphology and composition of the resulting materials deposited on glass, Si wafers and TiO_2 surfaces (using annealed Ti foils), were extensively characterized by scanning electron microscopy (SEM), high-resolution transmission electron microscope (HR-TEM), atomic force microscopy (AFM), X-ray spectroscopy (XPS), X-Ray diffraction (XRD) and Raman spectroscopy. The positive and promising results open a new path for the deposition of $MoSe_2$ on different supporting materials including all the benefits offered by ALD.

2. Methods

Two series of bis(trialkysilyl) ($R_3Si)_2Se$ and bis(trialkystannyl)selenides ($R_3Sn)_2Se$ have been synthesized by a two-step one-pot procedure as shown in Scheme 1. The developed methods A and B combine the observations made by Detty [71] and Syper [72], that differ in the *in-situ* preparation of Li_2Se. Whereas application of Superhydride (LiBHEt$_3$) proved to be more convenient and generally provides higher yield, a reaction of elemental Se and Li required longer reaction time and larger amount of diphenylacetylene. However, the latter proved to be less expensive, especially at large-scale production. The subsequent sluggish reaction of Li_2Se with trialkylsilylchlorides or trialkylstannylchlorides may significantly be accelerated by $BF_3.Et_2O$. The synthetic details and full characterization of Se precursors are provided in the Supplementary Data (SD). Their structures have been unambiguously confirmed by various analytical techniques, especially ^1H, ^{13}C, ^{29}Si, ^{119}Sn, and ^{77}Se nuclear magnetic resonance (NMR). The
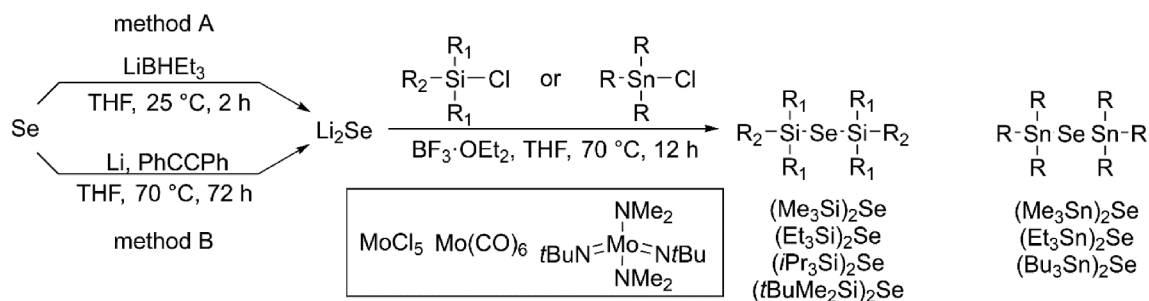
Scheme 1. Reaction pathways towards trialkylsilyl- and trialkylstannyl-Se precursors. The structure of used commercial Mo precursors is shown in the inset.
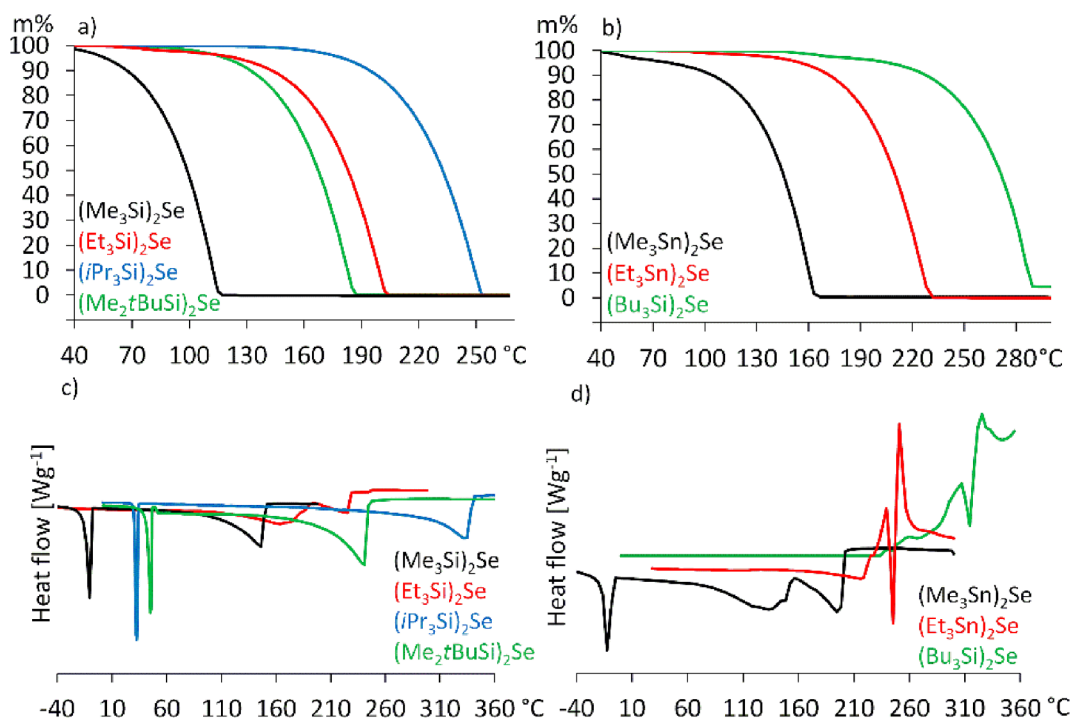
Fig. 1. TGA (up) and DSC (down) curves for bis(trialkylsilyl) selenides (left) and bis(trialkylstannyl)selenides (right).

corresponding NMR results are shown as Figs. S1 to S6 in the Supplementary Data file.

Thermal properties of the synthesized Se precursors were studied by thermal gravimetric analysis (TGA) and differential scanning calorimetry (DSC). Fig. 1 shows the corresponding thermograms, and the fundamental thermal parameters are summarized in Table S1. The Mo precursors $MoCl_5$ (Strem, anhydrous 99.6%), $Mo(CO)_6$ (Strem, 98%) and $Mo(NMe_2)_2$ $(NtBu)_2$ (Strem, 98%) were heated up to sufficiently high vapor pressure at 120 °C, 55 °C and 75 °C respectively, jointly with the Se precursors.

The ALD processes were carried out in a custom thermal ALD system at achamber pressure of 2 mbar applying different deposition temperatures as a function of the Mo precursor: $MoCl_5$ (300 °C), $Mo(CO)_6$ (167 °C) and $Mo(NMe_2)_2$ $(NtBu)_2$ (275 °C). The $MoSe_2$ deposition was explored using different substrates: Si wafer (with thin native SiO_2 on its surface), annealed Ti foils (with a thin anatase thermal TiO_2 layer on the foil surface) and a soda lime glass. Regardless the precursors used, the same ALD parameters were applied in all the processes. Thus, one growth ALD cycle was defined by the following sequence: Se precursor (400 ms) – N_2 purge (5 s) – Mo precursor (400 ms) – N_2 purge (5 s). The ALD process was initiated immediately after 5 pulses of ultrapure water (18 MΩ) were applied to increase the number of active sites on the substrates surface. The total number of ALD cycles was 400, unless stated otherwise. All processes used N_2 (99.999%) as a carrier gas at a flow rate of 40 standard cubic centimeter per minute (sccm).

The structure and morphology of the deposited $MoSe_2$ were characterized by field emission SEM (FE-SEM JEOL JSM 7500F) and a high-resolution transmission electron microscope (FEI Titan Themis 60, operated at 300 keV) equipped with a high angle annular dark field scanning transmission detector (HAADF-STEM). Proprietary Nanomeasure software was used to measure $MoSe_2$ interlayer distances and lattice spacing.

Phase Shift Image AFM mode was employed for simultaneous determination of topography and phase contrast by Solver Pro M AFM (NT-MDT; Russia) at air/room temperature condition with Au coated probe NSG-01 (typical resonance freq. 150 kHz, with the low force constant k < 2 N/m). The images were recorded at scan frequency

0.5 Hz for a resolution of 512 × 512 pixels for at least 3 independent areas. The $MoSe_2$ images were recorded with the minimal set point to avoid rupture of the $MoSe_2$ flakes oriented perpendicularly to the substrate. The majority of the flakes were broken even under these conditions with the cantileveŕs lowest force constant and the low set-point as supposed from the comparison of the AFM and the SEM scans. The topography was typified in the 3D scans for better notion of the top of the flakes and substrate at the same image. The samples were preserved under N_2 atmosphere after the ALD process and prior measurement.

The composition of $MoSe_2$ was monitored by X-ray photoelectron spectroscopy (XPS) (ESCA2SR, Scienta-Omicron) using a monochromatic Al Kα (1486.7 eV) X-ray source. The binding energy scale was referenced to adventitious carbon (284.8 eV). The quantitative analysis was performed using the elemental sensitivity factors provided by the manufacturer. X-ray diffraction analysis was carried out using Panalytical Empyrean with Cu tube and Pixel3D detector. Grazing incidence XRD was performed to obtain diffraction peaks of thin film. Incident angle was 1°. The patterns were recorded in range of 5 – 65°, step size was 0.026°.

Raman measurements were acquired by Raman micro-spectrometer HORIBA LabRAM HR Evolution system coupled by with a confocal microscope. Measurements were taken by 532 nm (green) laser excitation source in the range 100–500 cm^{-1}. All spectra were carefully corrected by baseline correction and noise reduction. Spikes were eliminated by spectra accumulation or manually in the LabSpec 6 software.

3. Results and discussion

Two series of bis(trialkysilyl) $(R_3Si)_2Se$ and bis(trialkystannyl)selenides $(R_3Sn)_2Se$ have been synthesized by two-step one-pot procedure as shown in Scheme 1. SEM characterization was used to study the structure and morphology of the $MoSe_2$ deposited on Si wafer, thin anatase TiO_2 layer and glass, upon ALD processes combining the different Se and Mo precursors introduced above in Scheme 1. ALD processes based on the use of $MoCl_5$ as Mo precursor and $(Me_3Si)_2Se$,

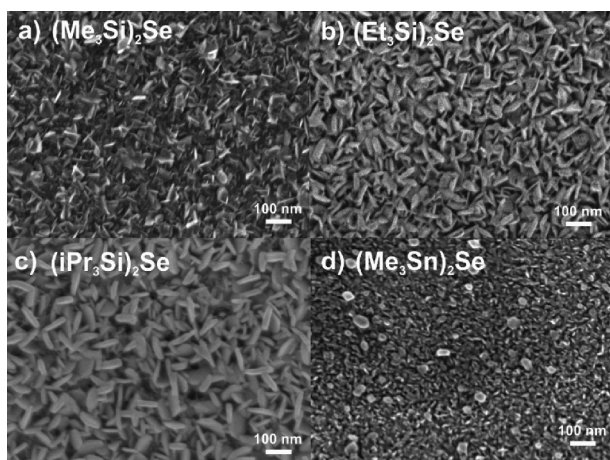**Fig. 2.** SEM top-view images of MoSe$_2$ nanostructures deposited on glass using MoCl$_5$ and different Se precursors: (a) (Me$_3$Si)$_2$Se (400 cycles), (b) (Et$_3$Si)$_2$Se (400 cycles), (c) (*i*Pr$_3$Si)$_2$Se (400 cycles), and (d) (Me$_3$Sn)$_2$Se (200 cycles).
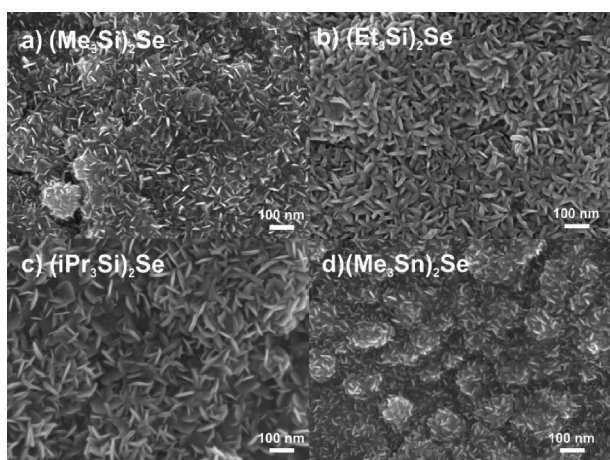

Fig. 3. SEM top-view images of MoSe$_2$ nanostructures deposited on thin anatase TiO$_2$ layer using MoCl$_5$ and different Se precursors: (a) (Me$_3$Si)$_2$Se (400 cycles), (b) (Et$_3$Si)$_2$Se (400 cycles), (c) (*i*Pr$_3$Si)$_2$Se (400 cycles), and (d) (Me$_3$Sn)$_2$Se (200 cycles).
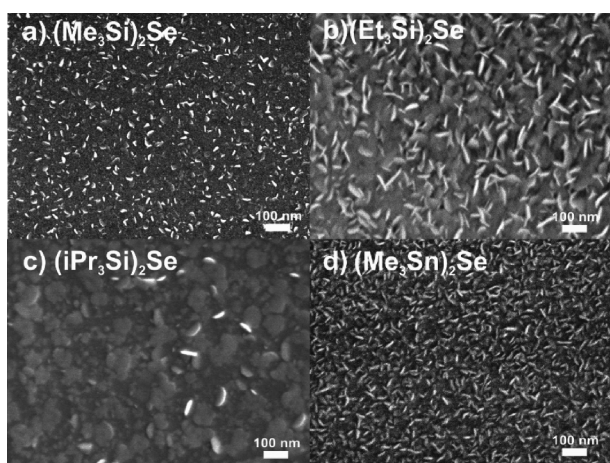

Fig. 4. SEM top view images of MoSe$_2$ nanostructures deposited on Si wafer using MoCl$_5$ and different Se precursor (a) (Me$_3$Si)$_2$Se (400 cycles), (b) (Et$_3$Si)$_2$Se (400 cycles), (c) (*i*Pr$_3$Si)$_2$Se (400 cycles), and (d) (Me$_3$Sn)$_2$Se (200 cycles).

(Et$_3$Si)$_2$Se, (*i*Pr$_3$Si)$_2$Se and (Me$_3$Sn)$_2$Se as Se precursor, exhibited vertically (out-of-plane) aligned flaky shaped nanosheets, as observed in previous works, where MoSe$_2$ was deposited by other techniques [26,27,31,38,51,59]. SEM images in Figs. 2–4 display flaky shaped MoSe$_2$ nanosheets on glass, thin anatase TiO$_2$ layer and Si wafer, respectively. Cross-sectional SEM images (see Fig. S7) confirmed the random out-of-plane orientation of the MoSe$_2$ flaky nanosheets. In contrast, the ALD processes using the rest of Se precursors, i.e. (*t*Bu-Me$_2$Si)$_2$Se, (Et$_3$Sn)$_2$Se and (Bu$_3$Sn)$_2$Se, did not result in vertically oriented sheets, but displayed totally different features instead, mainly comprised of granular structure or large particles, as shown in Fig. S8. Those unsuccessful MoSe$_2$ ALD processes can be ascribed to the thermal decomposition of the Se precursor (see Table S1) at the ALD process temperature (300 °C), as TGA analysis indicated in the Fig. 1. Unfortunately, the application of lower deposition temperatures using MoCl$_5$ is highly limited as it leads to clearly inferior reaction rates or total lack of chemical reaction between the precursors.

Regarding the ALD processes using both Mo(CO)$_6$ and [Mo(NMe$_2$)$_2$(N*t*Bu)$_2$] as Mo precursors, they did not lead to any deposited material, as shown in the illustrative optical pictures in Fig. S9. Therein, only the glass substrates corresponding to ALD processes using MoCl$_5$ exhibited the brownish color characteristic of the MoSe$_2$ deposition. ALD processes using the Mo(CO)$_6$ and [Mo(NMe$_2$)$_2$(N*t*Bu)$_2$] did not yield any MoSe$_2$ growth (as visible from totally transparent glass substrates and further confirmed by other characterization techniques). The poor growth or lack of growth obtained from Mo(CO)$_6$ and [Mo(NMe$_2$)$_2$(N*t*Bu)$_2$] compared to MoCl$_5$ can be explained based on their electron counts and electrophilic character. Whereas Mo(CO)$_6$ and [Mo(NMe$_2$)$_2$(N*t*Bu)$_2$] are relatively stable 18- and 12-electron complexes, MoCl$_5$ possesses 11 overall electrons. According to Lewis theory, its acidity and reactivity towards bis(trialkylsilyl) and bis(trialkylstannyl) selenides Se^{2-} (Lewis bases) is therefore higher. In addition, the polarized Mo-Cl bond present in MoCl$_5$ allows efficient Cl → Se exchange accompanied by the production of MoSe$_2$ and stable and volatile side products R$_3$SiCl or R$_3$SnCl that are easily removed through N$_2$ purging. Consequently, the results presented onwards will focus on the ALD processes based on the use of MoCl$_5$ as Mo precursor.

Detailed analysis of the as deposited MoSe$_2$ nanosheets was carried out by high-resolution transmission electron microscopy (HR-TEM) measurements. SEM cross section image shown in Fig. 5a illustrates the
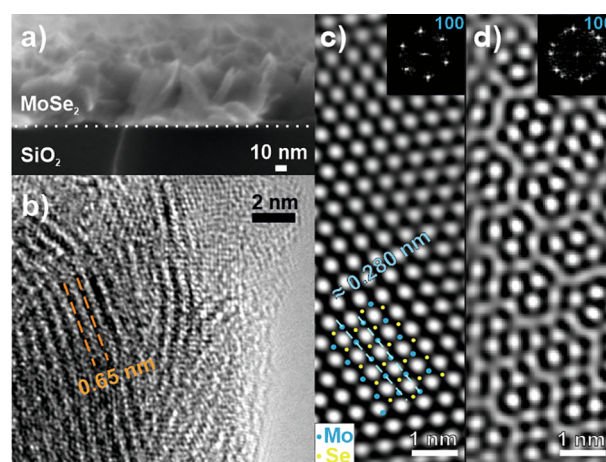

Fig. 5. (a) SEM cross section of Si wafer upon 600 MoSe$_2$ ALD cycles using MoCl$_5$ and (Me$_3$Si)$_2$Se. (b) HR-TEM image of a MoSe$_2$ nanoflake exhibiting 2D multi-layered structure. The calculated inter-layer spacing is 0.65 nm. High-resolution HR-TEM images of (c) monolayer, with schematic lattice structure, and (b) bilayer 2H MoSe$_2$ horizontal structures in high magnification. The Mo-Mo interatomic distance was ~ 0.280 nm. The insets in (c) and (d) show the Fast Fourier Transform patterns corresponding to mono and bilayered MoSe$_2$ structures, respectively.
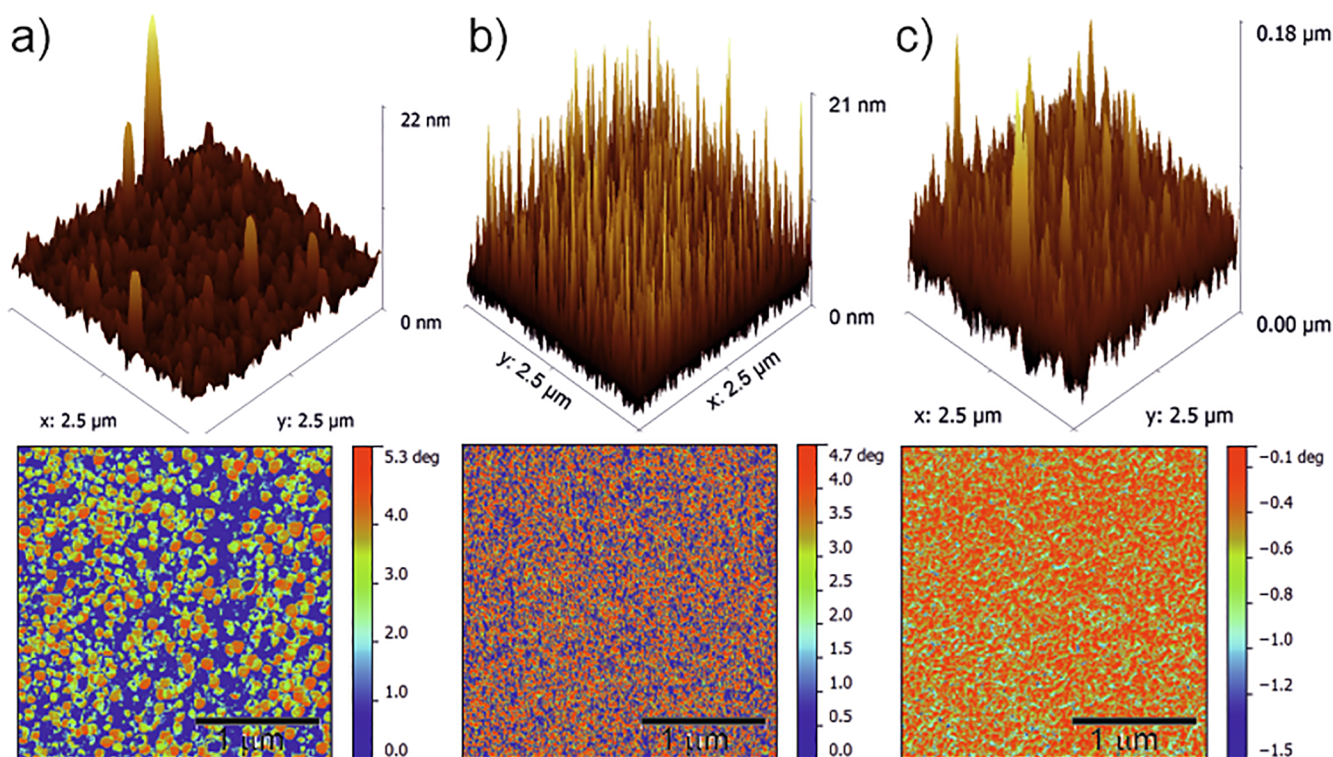
Fig. 6. 3D topography (top) and phase contrast (down) obtained from $MoSe_2$ deposited on Si wafer upon (a) 200, (b) 400 and (c) 600 $MoSe_2$ ALD cycles using $(Me_3Si)_2Se$ as Se precursor and $MoCl_5$ as Mo precursor.

$MoSe_2$ nanosheets morphology after 600 ALD cycles, complementing the previous SEM top view images and confirming unequivocally the random out-of-plane orientation. Fig. 5b is a HR-TEM image of 2D multilayered horizontal structure where the interlayer distance of ~ 0.65 nm is in total agreement with the one corresponding to the (0 0 2) plane of the hexagonal structure of $MoSe_2$ [73]. The images presented in Fig. 5c and d reveal the typical hexagonal structure of a monolayer and bilayer $MoSe_2$ respectively, along with a lattice spacing of ~0.280 nm corresponding to the (1 0 0) plane of $MoSe_2$ [43]. The Fast Fourier Transform (FFT) patterns showed in the insets of Fig. 5c and d confirmed the high crystallinity degree of the monolayer and bilayer structures corresponding to the (1 0 0) plane of 2H-$MoSe_2$.

AFM characterization provided further structural and morphological information that confirmed the morphology observed in the SEM top view images from Figs. 2–4. Fig. 6 displays how the growing evolution of the $MoSe_2$ nanosheets along with the number of the ALD cycles resulted in a dominant random out-of-plane orientation and an increasing surface coverage from ca. 55% (200 cycles) to 98% (600 cycles). The broken nanosheets were detected as the area with the increased phase contrast with respect to the substrate (see red sheets and blue substrate) due to the different adhesion and the density of the material similarly as previously reported [74,75]. The surface coverage increased with the number of ALD cycles and it was determined by the threshold technique of the phase image analysis of the standing and broken nano-sheets according to the literature [76,77].

The chemical composition of the $MoSe_2$ nanosheets deposited by $(Me_3Si)_2Se$, $(Et_3Si)_2Se$, $(iPr_3Si)_2Se$ and $(Me_3Sn)_2Se$ was analyzed by X-Ray photoelectron spectroscopy (XPS). Fig. S10 shows the corresponding XPS survey spectra. Fig. 7 shows the high resolution XPS spectra of Se and Mo species. In particular, Fig. 7(a) shows the spectrum of Se 3d, where the peaks located at 55.2 and 54.3 eV can be attributed to Se $3d_{3/2}$ and Se $3d_{5/2}$ of 2H $MoSe_2$ [73,78,79]. In the Fig. 7(b), the spectrum of Mo 3d displays two dominant peaks at 228.9 and 232 eV assigned to Mo $3d_{5/2}$ and Mo $3d_{3/2}$ and a minor broad Se 3 s state at

230 eV. The binding energies of Mo $3d_{5/2}$ and Mo $3d_{3/2}$ are consistent with the Mo^{+4} oxidation state of $MoSe_2$. These data are in agreement with previous literature about $MoSe_2$ [36,38,39]. No additional peaks attributed to oxidized forms Mo^{+5} and Mo^{+6} were observed. The XPS results obtained for the as deposited $MoSe_2$ on Si wafer and on thin anatase TiO_2 layer substrates displayed the same characteristic binding energies for Mo and Se assigned to $MoSe_2$ (shown in the Supplementary Data as Fig. S11), verifying the growth of $MoSe_2$ on these substrates, as observed in the corresponding SEM images. The corresponding $MoSe_2$ stoichiometry was evaluated by calculating the corresponding Se:Mo ratio showed in Table 1. The composition could be considered stoichiometric in case of the $(Me_3Si)_2Se$ and $(Et_3Si)_2Se$, while under-stoichiometric for the rest of the Se precursors. This sub-stoichiometric composition is ascribed to Se vacancies, influenced by process parameters, e.g., under saturated Se precursor dosing. The optimization of the ALD processes rendering sub-stoichiometric $MoSe_2$ was not within the scope of this study and will be addressed in further work.

Fig. 8 shows the GI-XRD patterns obtained from the $MoSe_2$ deposited on glass with the different Se precursors denoted in the legend. The diffraction peaks appearing at 2θ ~ 13.5°, 31.1° and 55° matched well with the (0 0 2), (1 0 0) and (1 1 0) planes of hexagonal (2H) $MoSe_2$ indicating the high purity of the $MoSe_2$. The higher intensity of the (0 0 2) peak as compared to the others confirms the $MoSe_2$ growth is predominantly along the c-axis as compared to in-plane orientation. This feature essentially agrees with the results observed from SEM and AFM characterizations. The intensity of the (0 0 2) peaks varies, indicating different degrees of crystallinity of the as deposited $MoSe_2$ by different Se precursors, while broader (0 0 2) peak would suggest both smaller size and fewer layers for the $MoSe_2$.

Raman spectroscopy is a paramount technique for the structural characterization of layered materials. Considering the group theory analysis, $MoSe_2$ belongs to the D_{6h} group characterized by four Raman-active modes, three in-plane E_{1g}, E_{2g}^1, and E_{2g}^2, and one out-of-plane A_{1g}. Fig. 9 shows representative Raman spectra of $MoSe_2$ deposited using

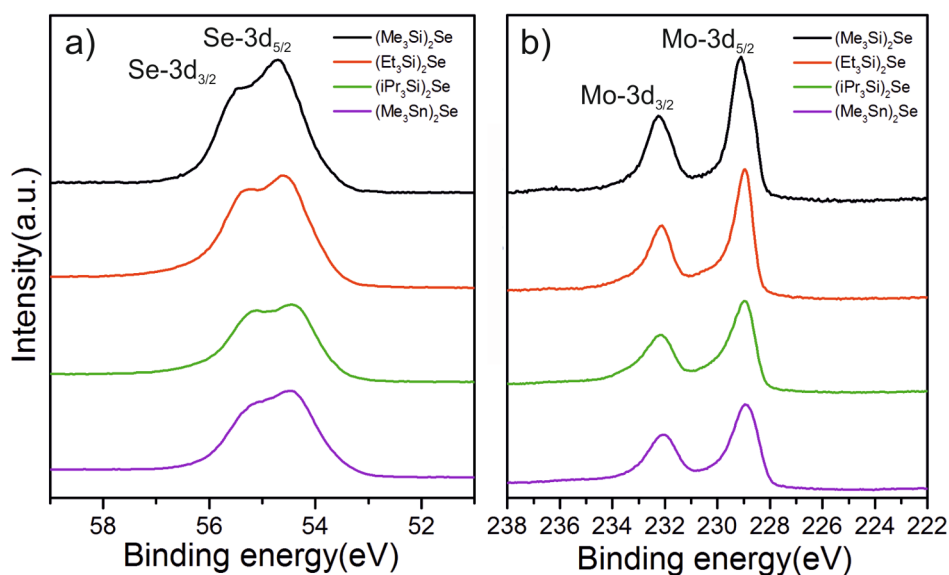**Fig. 7.** High-resolution XPS spectra of (a) Se 3d and (b) Mo 3d peaks corresponding to the MoSe$_2$ nanostructures deposited on glass using (Me$_3$Si)$_2$Se, (Et$_3$Si)$_2$Se, (iPr$_3$Si)$_2$Se and (Me$_3$Sn)$_2$Se precursors.

Table 1
The Se:Mo ratio calculated based on XPS analyses for the MoSe$_2$ grown on glass substrates from different Se precursors: (Me$_3$Si)$_2$Se, (Et$_3$Si)$_2$Se, (iPr$_3$Si)$_2$Se and (Me$_3$Sn)$_2$Se and MoCl$_5$ as Mo precursor.

Se precursor	Se/Mo ratio
(Me$_3$Si)$_2$Se	2.02
(Et$_3$Si)$_2$Se	1.92
(iPr$_3$Si)$_2$Se	1.56
(Me$_3$Sn)$_2$Se	1.74

the Se precursors (Me$_3$Si)$_2$Se, (Et$_3$Si)$_2$Se, (iPr$_3$Si)$_2$Se and (Me$_3$Sn)$_2$Se. Multiple lattice vibrational modes of MoSe$_2$ are observed confirming the polycrystalline nature of the MoSe$_2$. The characteristic peaks of MoSe$_2$, A$_{1g}$ (out-of-plane) and E$_{2g}^1$ (in-plane) modes, are observed at ~240 and ~289 cm^{-1}, respectively. Compared to the peaks position for bulk MoSe$_2$ (242 and 286 cm^{-1}), those modes exhibited red and blue shift, respectively, indicating few-layered nature of the deposited MoSe$_2$. As to the peak at ~350 cm^{-1}, it is assigned to the Raman-inactive mode A$_{2u}^2$ that becomes active in few-layer 2H-TMDs, as the crystal symmetry is lost along the c-axis. Likewise, the peak at ~169 cm^{-1} is associated with the E$_{1g}$ mode (inactive in bulk MoSe$_2$) but active for few-layered MoSe$_2$ due to resonance effect. Regarding the peaks *a* and *b*, as they do not correspond to any first order Raman process, they are attributed to second order Raman processes. Furthermore, the differences in the relative intensities between the modes A$_{1g}$ and E$_{2g}^1$ indicated the prevailing out-of-plane orientation over in-plane orientation of the MoSe$_2$ nanosheets in good agreement with previous results described above and published in the literature [80].

The use of different substrates allowed to evaluate the substrate influence on the ALD MoSe$_2$ growth. Fig. 10 shows SEM top view
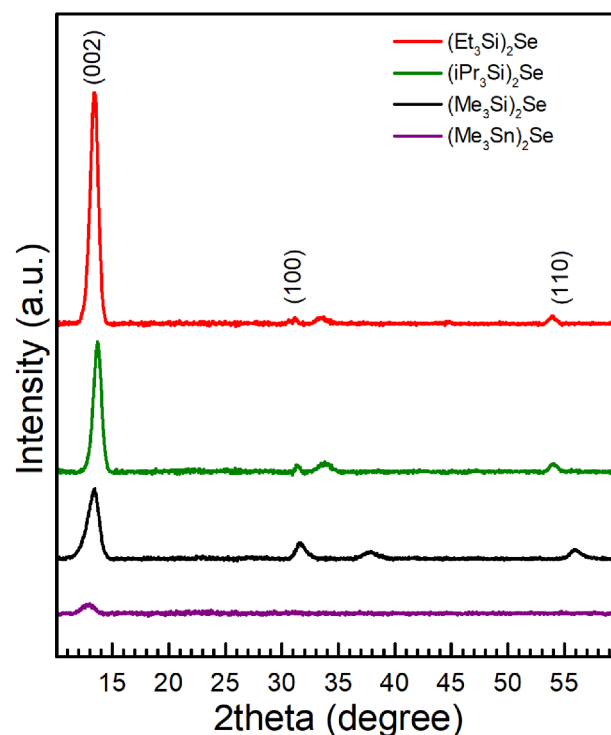

Fig. 8. XRD patterns of the MoSe$_2$ deposited on glass by the different Se precursors. The diffraction peaks are indicated in the XRD patterns.

images of the as deposited MoSe$_2$ on glass, thin anatase TiO$_2$ layer and Si wafer after 200, 400 and 600 ALD cycles. SEM images, after 200 ALD cycles, clearly demonstrate that the MoSe$_2$ growth is favored on glass over thin anatase TiO$_2$ layer and Si wafer. Interestingly, eventually (after 600 ALD cycles) out-of-plane randomly oriented MoSe$_2$ nanosheets were observed regardless the substrate nature, as reported in previous works [80,81]. It would indicate the MoSe$_2$ ALD growing mechanism is independent of the substrate nature. Thereby, the surface nature seems to strongly determine the number of the so-called active sites or nuclei on the substrate surface. These active sites act as the seeds where the material growth is initiated during the very early ALD
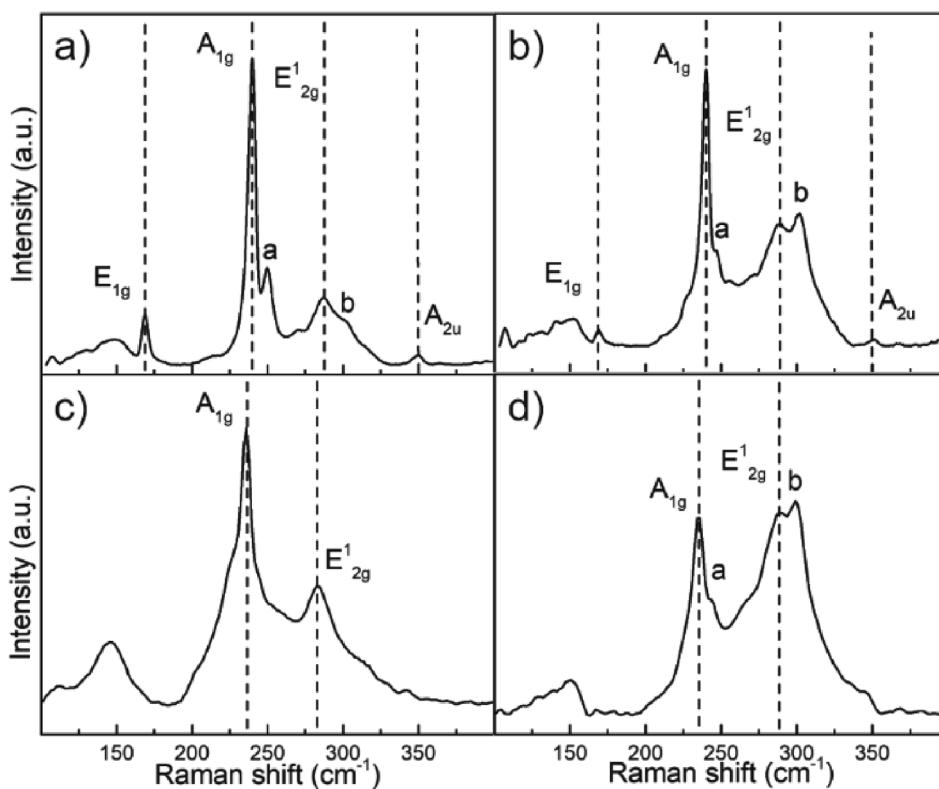
Fig. 9. Raman spectra of the MoSe₂ deposited on Si wafer using a) (Me₃Si)₂Se, b) (Et₃Si)₂Se, c) (iPr₃Si)₂Se, and d) (Me₃Sn)₂Se precursors and MoCl₅ as Mo precursor. The main peaks of in-plane and out-of-plane modes are referred.

stage.

In order to obtain an insight into the MoSe₂ growth during the very initial ALD stages, a detailed study was carried out based on performing MoSe₂ ALD processes applying 5, 10, 20 and 40 cycles on Si₃N₄ membranes using (Me₃Si)₂Se as Se precursor. The corresponding Si₃N₄

membranes were subsequently characterized by TEM. Low magnification TEM images in Fig. S12 (see Supplementary Data) exhibited a higher number of MoSe₂ nanoislands and an increased size of those along with a higher number of ALD cycles. EDX analysis (data not shown here) confirmed that the chemical composition of the
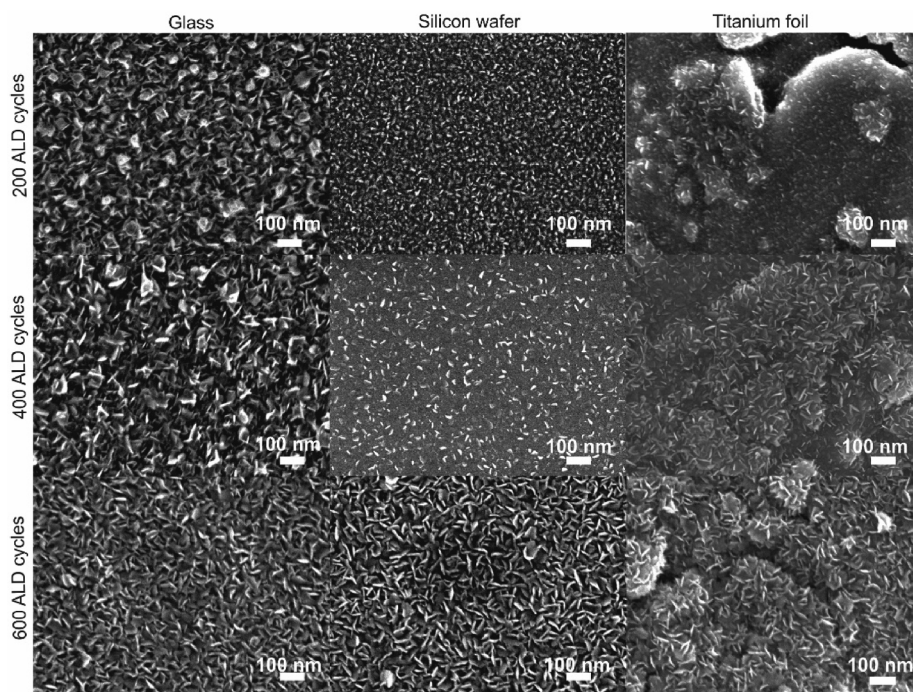

Fig. 10. SEM top-view images of MoSe₂ nanosheets grown using (Me₃Si)₂Se as Se precursor and MoCl₅ as Mo precursor on different substrates (glass, Si wafer and thin anatase TiO₂ upon applying different number of ALD cycles: 200, 400 and 600.
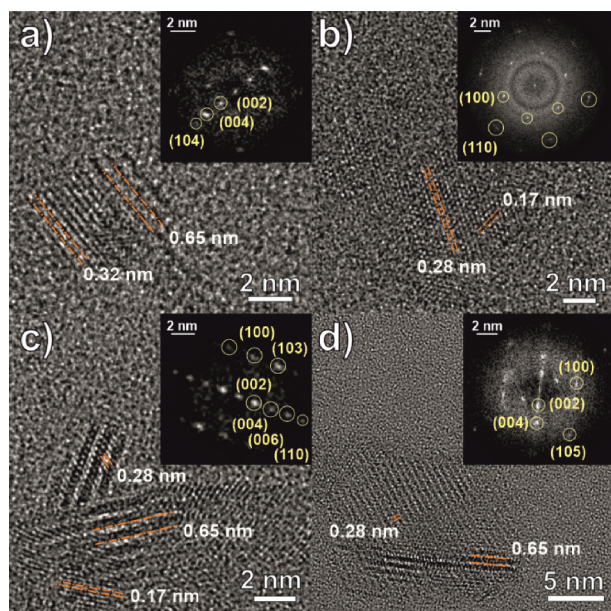
Fig. 11. HR-TEM images and the FFT patterns corresponding to $MoSe_2$ deposited on Si_3N_4 membranes upon (a) 5 ALD cycles, (b) 10 ALD cycles, (c) 20 ALD cycles, and (d) 40 ALD cycles. The coloured dotted lines are included to illustrate the different orientation of the $MoSe_2$ layers and the corresponding inter and intralayer distances. The Se and Mo precursors used were $(Me_3Si)_2Se$ and $MoCl_5$, respectively.

nanoislands corresponded to $MoSe_2$. Fig. 11 shows representative high-resolution TEM (HRTEM) images with the corresponding fast Fourier transform (FFT) patterns (inset) for every number of ALD cycles. Therein, island growth is observed, where $MoSe_2$ nanoisland size ranged from $\approx$ 2–3 nm for 5 ALD cycles up to $\approx$ 15 nm for 40 ALD cycles. The HRTEM images revealed diverse periodic atom arrangement of the as deposited $MoSe_2$ from the very early ALD stage. Thus, the Fig. 11a, corresponding to 5 ALD cycles, clearly displays multilayered structure with interlayer spacing of 0.65 nm and 0.32 nm, which matched well with the (0 0 2) and (0 0 4) plane of 2H hexagonal $MoSe_2$. The corresponding FFT pattern confirmed the presence of those crystal planes. In contrast to 5 ALD cycles, 10 ALD cycles showed unambiguously in-plane hexagonal $MoSe_2$ growth, as shown in Fig. 11b. Therein interlayer lattice spacing of 0.28 nm and 0.17 nm, assigned to the (1 0 0) and (1 1 0) planes, were identified, and further supported by the set of six-fold symmetry diffraction spots showed by the FFT pattern (inset). Interestingly, those results would point to concomitant growth of $MoSe_2$ adopting both in-plane and out-of-plane orientation during the very early stage of the ALD process. Indeed, such coexistence of $MoSe_2$ adopting in-plane and out-of-plane orientations was clearly visible by the HRTEM images and the corresponding FFT patterns in the Fig. 11c-d (20 and 40 ALD cycles, respectively). Those results provided a meaningful insight into the $MoSe_2$ growth evolution. Hence, $MoSe_2$ grows initially adopting concomitantly both in-plane and out-of-plane orientation. Nevertheless, as the number of ALD cycles increased, the random out-of-plane orientation becomes clearly dominant, as observed in Fig. 10.

Considering the literature, in order to rationalize the governing growing mechanism of out-of-plane orientation structures, different factors have been proposed. Kong et al. [80] synthesized $MoSe_2$ by selenization of e-beam evaporated Mo ultrathin films. They described that at the deposition temperature the diffusion of the precursors was found to be the rate-limiting process, and eventually the factor inducing the $MoSe_2$ out-of-plane orientation. Therein, as the diffusion through van der Waals gaps of the vertically aligned layers is expected faster than across the horizontal layers, the $MoSe_2$ would be prone to grow

perpendicularly oriented to the substrate. Previous works reported in 2D MoS_2 observing the same morphology evolution provide valuable insights that could be reasonably translated to $MoSe_2$ due to strongly similar chemical and morphological properties between both 2D materials. The collisions between growing MoS_2 islands cause the emergence of strain and compression forces, which would be released via structural distortion resulting in a vertical growth of the MoS_2 nanosheets [82]. Other factor to be noted is the presence of in-plane defects at the early growing stage (e.g., dislocation, vacancies, etc.) that would increase the surface energy and trigger the transition to vertical orientation in a more energetically stable form [83]. Those in-plane defects could be active sites for precursor adsorption acting as seeds for the growing of new MoS_2 nuclei [81]. Overall, it seems that the governing growing $MoSe_2$ mechanism could be due to a non-trivial interplay of several factors and a thorough study, out of the scope of this work, would be needed to shed more light on.

4. Conclusion

In summary, we synthesized and explored a set of alkysilyl $(R_3Si)_2Se$ and alkylstannyl $(R_3Sn)_2Se$ compounds as ALD Se precursors. These compounds were combined with different commercially available Mo precursors. Results showed that most alkysilyl compounds led to successful ALD deposition of $MoSe_2$. In contrast, the limited thermal stability of the alkylstannyl compounds reduced the ALD window of these molecules as Se precursors, with the exception of $(Me_3Sn)_2Se$. Extensive characterization of as deposited $MoSe_2$ via different techniques confirmed the growth of polycrystalline few layered $MoSe_2$ nanosheets oriented out-of-plane on substrates of different nature. In parallel, the $MoSe_2$ growth evolution from the very early ALD stage was explored by HRTEM. Results revealed island growth of 2H hexagonal $MoSe_2$ nanoislands, where the $MoSe_2$ initially adopted concomitantly both in-plane and out of plane orientations. Eventually, as the number of ALD cycles increases, the random out-of-plane orientation of the $MoSe_2$ nanosheets becomes clearly dominant. The application of ALD $MoSe_2$ into a device and the corresponding performance in different applications is currently ongoing and will be reported in a following work. Therefore, this work introduces a set of Se ALD precursors enabling to extend the use of ALD for the deposition of $MoSe_2$ with all the benefits of ALD technique, including precise control over composition and thickness as well as uniformity on the substrate regardless of the shape.

Appendix A. Supplementary data

Supplementary data to this article can be found online at https://doi.org/10.1016/j.flatc.2020.100166.

References

[1] K.S. Novoselov, A.K. Geim, S.V. Morozov, D. Jiang, Y. Zhang, S.V. Dubonos, I.V. Grigorieva, A.A. Firsov, Electric field in atomically thin carbon films, Science 336 (2004) 666–669, https://doi.org/10.1126/science.1102896.
[2] X. Huang, Z. Yin, S. Wu, X. Qi, Q. He, Q. Zhang, Q. Yan, F. Boey, H. Zhang, Graphene-based materials: synthesis, characterization, properties, and applications, Small 7 (2011) 1876–1902, https://doi.org/10.1002/smll.201002009.
[3] P. Avouris, C. Dimitrakopoulos, Graphene: synthesis and applications, Mater. Today

15 (2012) 86–97, https://doi.org/10.1016/S1369-7021(12)70044-5.

[4] J.H. Warner, F. Schaffel, M. Rummeli, A. Bachmatiuk, F. Schäffel, A. Bachmatiuk, M.H. Rümmeli, Graphene fundamentals and emergent applications, Graphene 29 (2013) 954–965, https://doi.org/10.1016/B978-0-12-394593-8.00001-1.

[5] M. Pumera, Graphene-based nanomaterials for energy storage, Energy Environ. Sci. 4 (2011) 668–674, https://doi.org/10.1039/c0ee00295j.

[6] W. Choi, N. Choudhary, G.H. Han, J. Park, D. Akinwande, Y.H. Lee, Recent development of two-dimensional transition metal dichalcogenides and their applications, Mater. Today 20 (2017) 116–130, https://doi.org/10.1016/j.mattod.2016.10.002.

[7] S. Manzeli, D. Ovchinnikov, D. Pasquier, O.V. Yazyev, A. Kis, 2D transition metal dichalcogenides, Nat. Rev. Mater. 2 (2017) 17033, https://doi.org/10.1038/natrevmats.2017.33.

[8] K.F. Mak, J. Shan, Photonics and optoelectronics of 2D semiconductor transition metal dichalcogenides, Nat. Photonics 10 (2016) 216–226, https://doi.org/10.1038/nphoton.2015.282.

[9] W. Zheng, Y. Jiang, X. Hu, H. Li, Z. Zeng, X. Wang, Light emission properties of 2D transition metal dichalcogenides: fundamentals and applications, Adv. Opt. Mater. 6 (2018) 1–29, https://doi.org/10.1002/adom.201800420.

[10] J. Ping, Z. Fan, M. Sindoro, Y. Ying, H. Zhang, Recent advances in sensing applications of two-dimensional transition metal dichalcogenide nanosheets and their composites, Adv. Funct. Mater. 27 (2017) 1605817, https://doi.org/10.1002/adfm.201605817.

[11] M. Donarelli, L. Ottaviano, 2D materials for gas sensing applications: a review on graphene oxide, MoS_2, WS_2 and phosphorene, Sensors 18 (2018) 3638, https://doi.org/10.3390/s18113638.

[12] S. Zhang, W. Zhang, T.H. Nguyen, J. Jian, W. Yang, Synthesis of molybdenum diselenide nanosheets and its ethanol-sensing mechanism, Mater. Chem. Phys. 222 (2019) 139–146, https://doi.org/10.1016/j.matchemphys.2018.08.062.

[13] M. Pumera, Z. Sofer, A. Ambrosi, Layered transition metal dichalcogenides for electrochemical energy generation and storage, J. Mater. Chem. A 2 (2014) 8981–8987, https://doi.org/10.1039/c4ta00652f.

[14] H.H. Li, Y. Shi, M.H. Chiu, L.J. Li, Q. Lu, Y. Yu, Q. Ma, B. Chen, H. Zhang, H. Jin, C. Guo, X. Liu, J. Liu, A. Vasile, Y. Jiao, Y. Zheng, S. Qiao, Z. Li, S.L. Wong, H. Zhang, Z. Wu, G. Tai, X.X. Wang, T. Hu, W. Zheng, Y. Jiang, X. Hu, H.H. Li, Z. Zeng, X.X. Wang, K.F. Mak, J. Shan, B. Luo, G. Liu, L. Wang, D. Geng, H.Y. Yang, W. Choi, N. Choudhary, G.H. Han, J. Park, D. Akinwande, Y.H. Lee, J.R. Brent, N. Savjani, P.O. Brien, Emerging energy applications of two-dimensional layered transition metal dichalcogenides, Nano Energy 18 (2015) 293–305, https://doi.org/10.1016/j.nanoen.2015.10.023.

[15] Q. Lu, Y. Yu, Q. Ma, B. Chen, H. Zhang, 2D transition-metal-dichalcogenide-nanosheet-based composites for photocatalytic and electrocatalytic hydrogen evolution reactions, Adv. Mater. 28 (2016) 1917–1933, https://doi.org/10.1002/adma.201503270.

[16] D.M. Andoshe, J.M. Jeon, S.Y. Kim, H.W. Jang, Two-dimensional transition metal dichalcogenide nanomaterials for solar water splitting, Electron. Mater. Lett. 11 (2015) 323–335, https://doi.org/10.1007/s13391-015-4402-9.

[17] B. Luo, G. Liu, L. Wang, Recent advances in 2D materials for photocatalysis, Nanoscale 8 (2016) 6904–6920, https://doi.org/10.1039/C6NR00546B.

[18] H. Jin, C. Guo, X. Liu, J. Liu, A. Vasileff, Y. Jiao, Y. Zheng, S. Qiao, Emerging two-dimensional nanomaterials for electrocatalysis, Chem. Rev. 118 (2018) 6337–6408, https://doi.org/10.1021/acs.chemrev.7b00689.

[19] X. Chia, A. Ambrosi, Z. Sofer, J. Luxa, M. Pumera, Catalytic and charge transfer properties of transition metal dichalcogenides arising from electrochemical pre-treatment, ACS Nano 9 (2015) 5164–5179, https://doi.org/10.1021/acsnano.5b00501.

[20] C. Li, Q. Cao, F. Wang, Y. Xiao, Y. Li, J.J. Delaunay, H. Zhu, Engineering graphene and TMDs based van der Waals heterostructures for photovoltaic and photoelectrochemical solar energy conversion, Chem. Soc. Rev. 47 (2018) 4981–5037, https://doi.org/10.1039/c8cs00067k.

[21] C. Zhu, D. Gao, J. Ding, D. Chao, J. Wang, TMD-based highly efficient electrocatalysts developed by combined computational and experimental approaches, Chem. Soc. Rev. 47 (2018) 4332–4356, https://doi.org/10.1039/c7cs00705a.

[22] P. Luo, F. Zhuge, Q. Zhang, Y. Chen, L. Lv, Y. Huang, H. Li, T. Zhai, Doping engineering and functionalization of two-dimensional metal chalcogenides, Nanoscale Horizons 4 (2019) 26–51, https://doi.org/10.1039/c8nh00150b.

[23] D. Sarkar, X. Xie, J. Kang, H. Zhang, W. Liu, J. Navarrete, M. Moskovits, K. Banerjee, Functionalization of transition metal dichalcogenides with metallic nanoparticles: Implications for doping and gas-sensing, Nano Lett. 15 (2015) 2852–2862, https://doi.org/10.1021/nl504454u.

[24] A. Eftekhari, Molybdenum diselenide (MoSe2) for energy storage, catalysis, and optoelectronics, Appl. Mater. Today 8 (2017) 1–17, https://doi.org/10.1016/j.apmt.2017.01.006.

[25] Y. Liu, M. Zhu, D. Chen, Sheet-like $MoSe_2$/C composites with enhanced Li-ion storage properties, J. Mater. Chem. A 3 (2015) 11857–11862, https://doi.org/10.1039/c5ta02100f.

[26] J. Yao, B. Liu, S. Ozden, J. Wu, S. Yang, M.T.F. Rodrigues, K. Kalaga, P. Dong, P. Xiao, Y. Zhang, R. Vajtai, P.M. Ajayan, 3D nanostructured molybdenum diselenide/graphene foam as anodes for long-cycle life lithium-ion batteries, Electrochim. Acta 176 (2015) 103–111, https://doi.org/10.1016/j.electacta.2015.06.138.

[27] L. Ma, X. Zhou, L. Xu, X. Xu, L. Zhang, W. Chen, Ultrathin few-layered molybdenum selenide/graphene hybrid with superior electrochemical Li-storage performance, J. Power Sources 285 (2015) 274–280, https://doi.org/10.1016/j.jpowsour.2015.03.120.

[28] Z. Zhang, Y. Fu, X. Yang, Y. Qu, Z. Zhang, Hierarchical $MoSe_2$ nanosheets/reduced graphene oxide composites as anodes for lithium-ion and sodium-ion batteries with enhanced electrochemical performance, ChemNanoMat. 1 (2015) 409–414, https://doi.org/10.1002/cnma.201500097.

[29] Z. Zhang, X. Yang, Y. Fu, K. Du, Ultrathin molybdenum diselenide nanosheets anchored on multi-walled carbon nanotubes as anode composites for high performance sodium-ion batteries, J. Power Sources 296 (2015) 2–9, https://doi.org/10.1016/j.jpowsour.2015.07.008.

[30] M. Ojha, M. Deepa, Molybdenum selenide nanotubes decorated carbon net for a high performance supercapacitor, Chem. Eng. J. 368 (2019) 772–783, https://doi.org/10.1016/j.cej.2019.03.002.

[31] V.K. Mariappan, K. Krishnamoorthy, P. Pazhamalai, S. Sahoo, S.J. Kim, Electrodeposited molybdenum selenide sheets on nickel foam as a binder-free electrode for supercapacitor application, Electrochim. Acta 265 (2018) 514–522, https://doi.org/10.1016/j.electacta.2018.01.075.

[32] P. Pazhamalai, K. Krishnamoorthy, S. Sahoo, S.J. Kim, Two-dimensional molybdenum diselenide nanosheets as a novel electrode material for symmetric supercapacitors using organic electrolyte, Electrochim. Acta 295 (2019) 591–598, https://doi.org/10.1016/j.electacta.2018.10.191.

[33] B. Kirubasankar, P. Palanisamy, S. Arunachalam, V. Murugadoss, S. Angaiah, 2D $MoSe_2$ -Ni(OH)$_2$ nanohybrid as an efficient electrode material with high rate capability for asymmetric supercapacitor applications, Chem. Eng. J. 355 (2019) 881–890, https://doi.org/10.1016/j.cej.2018.08.185.

[34] H. Tang, H. Huang, X. Wang, K. Wu, G. Tang, C. Li, Hydrothermal synthesis of 3D hierarchical flower-like $MoSe_2$ microspheres and their adsorption performances for methyl orange, Appl. Surf. Sci. 379 (2016) 296–303, https://doi.org/10.1016/j.apsusc.2016.04.086.

[35] X. Yang, R. Wu, H. Liu, H. Fan, H. Zhang, Y. Sun, Amorphous molybdenum selenide as highly efficient photocatalyst for the photodegradation of organic dyes under visible light, Appl. Surf. Sci. 457 (2018) 214–220, https://doi.org/10.1016/j.apsusc.2018.06.039.

[36] X. Zheng, L. Yang, Y. Li, L. Yang, S. Luo, Direct Z-scheme $MoSe_2$ decorating TiO_2 nanotube arrays photocatalyst for water decontamination, Electrochim. Acta 298 (2019) 663–669, https://doi.org/10.1016/j.electacta.2018.12.130.

[37] N.T. Shelke, D.J. Late, Hydrothermal growth of MoSe2 nanoflowers for photo- and humidity sensor applications, Sensors Actuat. A-Phys. 295 (2019) 160–168, https://doi.org/10.1016/j.sna.2019.05.045.

[38] Y. Huang, Y.E. Miao, J. Fu, S. Mo, C. Wei, T. Liu, Perpendicularly oriented few-layer $MoSe_2$ on SnO_2 nanotubes for efficient hydrogen evolution reaction, J. Mater. Chem. A 3 (2015) 16263–16271, https://doi.org/10.1039/c5ta03704b.

[39] Z. Lei, S. Xu, P. Wu, Ultra-thin and porous $MoSe_2$ nanosheets: facile preparation and enhanced electrocatalytic activity towards the hydrogen evolution reaction, Phys. Chem. Chem. Phys. 18 (2016) 70–74, https://doi.org/10.1039/c5cp06483j.

[40] Y. Huang, H. Lu, H. Gu, J. Fu, S. Mo, C. Wei, Y.-E. Miao, T. Liu, A CNT@$MoSe_2$ hybrid catalyst for efficient and sTable hydrogen evolution, Nanoscale 7 (2015) 18595–18602, https://doi.org/10.1039/C5NR05739F.

[41] B. Mao, T. Bao, J. Yu, L. Zheng, J. Qin, W. Yin, M. Cao, One-pot synthesis of $MoSe_2$ hetero-dimensional hybrid self-assembled by nanodots and nanosheets for electrocatalytic hydrogen evolution and photothermal therapy, Nano Res. 10 (2017) 2667–2682, https://doi.org/10.1007/s12274-017-1469-7.

[42] C. Dai, Z. Zhou, C. Tian, Y. Li, C. Yang, X. Gao, X. Tian, Large-scale synthesis of graphene-like $MoSe_2$ nanosheets for efficient hydrogen evolution reaction, J. Phys. Chem. C 121 (2017) 1974–1981, https://doi.org/10.1021/acs.jpcc.6b11423.

[43] N.K. Oh, C. Kim, J. Lee, O. Kwon, Y. Choi, G.Y. Jung, H.Y. Lim, S.K. Kwak, G. Kim, H. Park, In-situ local phase-transitioned $MoSe_2$ in $La_{0.5}Sr_{0.5}CoO_{3-\delta}$ heterostructure and stable overall water electrolysis over 1000 hours, Nat. Commun. 10 (2019) 1–12, https://doi.org/10.1038/s41467-019-09339-y.

[44] S. Kou, X. Guo, X. Xu, J. Yang, TiO_2 on $MoSe_2$ nanosheets as an advanced photocatalyst for hydrogen evolution in visible light, Catal. Commun. 106 (2018) 60–63, https://doi.org/10.1016/j.catcom.2017.12.013.

[45] L. Najafi, S. Bellani, R. Oropesa-Nuniez, M. Prato, B. Martín-García, R. Brescia, F. Bonaccorso, Carbon nanotube-supported $MoSe_2$ holey flake:Mo_2 C ball hybrids for bifunctional pH-universal water splitting, ACS Nano 13 (2019) 3162–3176, https://doi.org/10.1021/acsnano.8b08670.

[46] S. Hussain, D. Vikraman, K. Akbar, B.A. Naqvi, S.M. Abbas, H.S. Kim, S.H. Chun, J. Jung, Fabrication of $MoSe_2$ decorated three-dimensional graphene composites structure as a highly stable electrocatalyst for improved hydrogen evolution reaction, Renew. Energy 143 (2019) 1659–1669, https://doi.org/10.1016/j.renene.2019.05.126.

[47] L. Wu, S. Shi, Q. Li, X. Zhang, X. Cui, TiO_2 nanoparticles modified with 2D $MoSe_2$ for enhanced photocatalytic activity on hydrogen evolution, Int. J. Hydrogen Energy 44 (2019) 720–728, https://doi.org/10.1016/j.ijhydene.2018.10.214.

[48] J.R. Brent, N. Savjani, P.O. Brien, Progress in materials science synthetic approaches to two-dimensional transition metal dichalcogenide nanosheets, Prog. Mater. Sci. 89 (2017) 411–478, https://doi.org/10.1016/j.pmatsci.2017.06.002.

[49] C.T. Nguyen, T.M. Duong, M. Nguyen, Q.T. Nguyen, A.D. Nguyen, U.T. Dieu Thuy, Q.D. Truong, T.T. Nguyen, Q.L. Nguyen, P.D. Tran, Structure and electrochemical property of amorphous molybdenum selenide H_2-evolving catalysts prepared by a solvothermal synthesis, Int. J. Hydrogen Energy 44 (2019) 13273–13283, https://doi.org/10.1016/j.ijhydene.2019.03.186.

[50] M. Jiang, J. Zhang, M. Wu, W. Jian, H. Xue, T.W. Ng, C.S. Lee, J. Xu, Synthesis of 1T- $MoSe_2$ ultrathin nanosheets with an expanded interlayer spacing of 1.17 nm for efficient hydrogen evolution reaction, J. Mater. Chem. A 4 (2016) 14949–14953, https://doi.org/10.1039/c6ta07020e.

[51] B. Kirubasankar, S. Vijayan, S. Angaiah, Sonochemical synthesis of a 2D–2D $MoSe_2$ /graphene nanohybrid electrode material for asymmetric supercapacitors, Sustain. Energy Fuels 3 (2019) 467–477, https://doi.org/10.1039/c8se00446c.

[52] N.D. Boscher, C.J. Carmalt, R.G. Palgrave, J.J. Gil-Tomas, I.P. Parkin, Atmospheric pressure CVD of molybdenum diselenide films on glass, Chem. Vap. Depos. 12 (2006) 692–698, https://doi.org/10.1002/cvde.200606502.

[53] X. Lu, M.I.B. Utama, J. Lin, X. Gong, J. Zhang, Y. Zhao, S.T. Pantelides, J. Wang, Z. Dong, Z. Liu, W. Zhou, Q. Xiong, Large-area synthesis of monolayer and few-layer MoSe₂ films on SiO₂ substrates, Nano Lett. 14 (2014) 2419–2425, https://doi.org/10.1021/nl5000906.

[54] R. Ghosh, J.S. Kim, A. Roy, H. Chou, M. Vu, S.K. Banerjee, D. Akinwande, Large area chemical vapor deposition growth of monolayer MoSe₂ and its controlled sulfurization to MoS₂, J. Mater. Res. 31 (2016) 917–922, https://doi.org/10.1557/jmr.2016.7.

[55] C. Jung, S.M. Kim, H. Moon, G. Han, J. Kwon, Y.K. Hong, I. Omkaram, Y. Yoon, S. Kim, J. Park, Highly crystalline CVD-grown multilayer MoSe₂ thin film transistor for fast photodetector, Sci. Rep. 5 (2015) 1–9, https://doi.org/10.1038/srep15313.

[56] J. Yin, H. Chen, W. Lu, M. Liu, I. Ling Li, M. Zhang, W. Zhang, J. Wang, Z. Xu, P. Yan, W. Liu, S. Ruan, Large-area and highly crystalline MoSe₂ for optical modulator, 484001, Nanotechnology 28 (2017), https://doi.org/10.1088/1361-6528/aa9535.

[57] Y. Zhang, H. Zhu, L. Yu, J. He, C. Huang, MoSe2 modified TiO₂ nanotube arrays with superior photoelectrochemical performance, Mater. Res. Express 5 (2018) 045014, , https://doi.org/10.1088/2053-1591/aab90c.

[58] X. Chia, M. Pumera, Inverse opal-like porous MoSe_x films for hydrogen evolution catalysis: overpotential-pore size dependence, ACS Appl. Mater. Interfaces 10 (2018) 4937–4945, https://doi.org/10.1021/acsami.7b17800.

[59] B.B. Wang, M.K. Zhu, I. Levchenko, K. Zheng, B. Gao, S. Xu, K. Ostrikov, Effects of hydrogen on the structural and optical properties of MoSe₂ grown by hot filament chemical vapor deposition, J. Cryst. Growth 475 (2017) 1–9, https://doi.org/10.1016/j.jcrysgro.2017.05.024.

[60] B.B. Wang, M.K. Zhu, K. Ostrikov, R.W. Shao, K. Zheng, Structure and photoluminescence of molybdenum selenide nanomaterials grown by hot filament chemical vapor deposition, J. Alloys Compd. 647 (2015) 734–739, https://doi.org/10.1016/j.jallcom.2015.05.237.

[61] C.F. Tsang, M.A. Ledina, J.L. Stickney, Molybdenum diselenide formation using electrochemical atomic layer deposition (E-ALD), J. Electroanal. Chem. 793 (2017) 242–249, https://doi.org/10.1016/j.jelechem.2017.01.065.

[62] U. Gupta, B.S. Naidu, U. Maitra, A. Singh, S.N. Shirodkar, U.V. Waghmare, C.N.R. Rao, Characterization of few-layer 1T- MoSe₂ and its superior performance in the visible-light induced hydrogen evolution reaction, APL Mater. 2 (2014) 092802, , https://doi.org/10.1063/1.4892976.

[63] N. Rohaizad, C.C. Mayorga-Martinez, Z. Sofer, M. Pumera, 1T-phase transition metal dichalcogenides (MoS₂, MoSe₂, WS₂, and WSe₂) with fast heterogeneous electron transfer: application on second-generation enzyme-based biosensor, ACS Appl. Mater. Interfaces 9 (2017) 40697–40706, https://doi.org/10.1021/acsami.7b13090.

[64] J. Zhang, Y. Chen, M. Liu, K. Du, Y. Zhou, Y. Li, Z. Wang, J. Zhang, 1T@2H- MoSe₂ nanosheets directly arrayed on Ti plate: an efficient electrocatalytic electrode for hydrogen evolution reaction, Nano Res. 11 (2018) 4587–4598, https://doi.org/10.1007/s12274-018-2040-x.

[65] Y. Yu, G.H. Nam, Q. He, X.J. Wu, K. Zhang, Z. Yang, J. Chen, Q. Ma, M. Zhao, Z. Liu, F.R. Ran, X. Wang, H. Li, X. Huang, B. Li, Q. Xiong, Q. Zhang, Z. Liu, L. Gu, Y. Du, W. Huang, H. Zhang, High phase-purity 1T′-MoS₂ - and 1T′- MoSe₂-layered crystals, Nat. Chem. 10 (2018) 638–643, https://doi.org/10.1038/s41557-018-0035-6.

[66] F. Cheng, Z. Hu, H. Xu, Y. Shao, J. Su, Z. Chen, W. Ji, K.P. Loh, Interface engineering of Au(111) for the growth of 1T′-MoSe₂, ACS Nano 13 (2019) 2316–2323, https://doi.org/10.1021/acsnano.8b09054.

[67] S.M. George, Atomic layer deposition: an overview, Chem. Rev. 110 (2010) 111–131, https://doi.org/10.1021/cr900056b.

[68] V. Pore, T. Hatanpää, M. Ritala, M. Leskela, Atomic layer deposition of metal tellurides and selenides using alkylsilyl compounds of tellurium and selenium, J. Am. Chem. Soc. 131 (2009) 3478–3480, https://doi.org/10.1021/ja8090388.

[69] R.G. Gordon, Introduction to ALD precursors and reaction mechanisms tutorial for ALD, At. Layer Depos. Semicond. (2014), https://doi.org/10.1007/978-1-4614-8054-9_2.

[70] M. Krbal, J. Prikryl, R. Zazpe, F. Dvorak, F. Bures, J.M. Macak, 2D MoSe₂ structures prepared by atomic layer deposition, Phys. Status Solidi - Rapid Res. Lett. 12 (2018) 1800023, https://doi.org/10.1002/pssr.201800023.

[71] M.R. Detty, M.D. Seidler, Bis(trialkylsilyl) chalcogenides. 1. Preparation and reduction of group 6A oxides, J. Org. Chem. 47 1354–1356 (1982), https://doi.org/10.1021/jo00346a041.

[72] L. Syper, J. Mlochowski, Lithium diselenide in aprotic medium - a convenient reagent for synthesis of organic diselenides, Tetrahedron 44 (1988) 6119–6130, https://doi.org/10.1016/S0040-4020(01)89801-X.

[73] S. Deng, Y. Zhong, Y. Zeng, Y. Wang, Z. Yao, F. Yang, S. Lin, X. Wang, X. Lu, X. Xia, J. Tu, Directional construction of vertical nitrogen-doped 1T–2H MoSe₂/graphene shell/core nanoflake arrays for efficient hydrogen evolution reaction, Adv. Mater. 29 (2017) 1700748, https://doi.org/10.1002/adma.201700748.

[74] P. Knotek, E. Chanova, F. Rypacek, AFM imaging and analysis of local mechanical properties for detection of surface pattern of functional groups, Mater. Sci. Eng. C 33 (2013) 1963–1968, https://doi.org/10.1016/j.msec.2013.01.006.

[75] R. García, R. Pérez, Dynamic atomic force microscopy methods, Surf. Sci. Rep. 47 (2002) 197–301, https://doi.org/10.1016/S0167-5729(02)00077-8.

[76] P.K. Sahoo, P. Soltani, A.K.C. Wong, A survey of thresholding techniques, Lect. Notes Comput. Sc. 41 (1988) 230–266, https://doi.org/10.1016/0734-189X(88)90022-9.

[77] P. Knotek, M. Vlcek, M. Kincl, L. Tichy, On the ultraviolet light induced oxidation of amorphous As₂S₃ film, Thin Solid Films 520 (2012) 5472–5478, https://doi.org/10.1016/j.tsf.2012.03.116.

[78] A. Ambrosi, Z. Sofer, M. Pumera, 2H → 1T phase transition and hydrogen evolution activity of MoS2, MoSe2, WS2 and WSe2 strongly depends on the MX2 composition, Chem. Commun. 51 (2015) 8450–8453, https://doi.org/10.1039/C5CC00803D.

[79] Y. Qu, H. Medina, S.-W. Wang, Y.-C. Wang, C.-W. Chen, T.-Y. Su, A. Manikandan, K. Wang, Y.-C. Shih, J.-W. Chang, H.-C. Kuo, C.-Y. Lee, S.-Y. Lu, G. Shen, Z.M. Wang, Y.-L. Chueh, Wafer scale phase-engineered 1T- and 2H-MoSe₂/Mo core-shell 3D-hierarchical nanostructures toward efficient electrocatalytic hydrogen evolution reaction, Adv. Mater. 28 (2016) 9831–9838, https://doi.org/10.1002/adma.201602697.

[80] D. Kong, H. Wang, J.J. Cha, M. Pasta, K.J. Koski, J. Yao, Y. Cui, Synthesis of MoS₂ and MoSe₂ films with vertically aligned layers, Nano Lett. 13 (3) (2013) 1341–1347, https://doi.org/10.1021/nl400258t.

[81] A. Sharma, M.A. Verheijen, L. Wu, S. Karwal, V. Vandalon, H.C.M. Knoops, R.S. Sundaram, J.P. Hofmann, W.M.M. Kessels, A.A. Bol, Low-temperature plasma-enhanced atomic layer deposition of 2-D MoS2: Large area, thickness control and tuneable morphology, Nanoscale 10 (2018) 8615–8627, https://doi.org/10.1039/c8nr02339e.

[82] H. Li, H. Wu, S. Yuan, H. Qian, Synthesis and characterization of vertically standing MoS₂ nanosheets, Sci. Rep. 6 (2016) 21171, https://doi.org/10.1038/srep21171.

[83] L. Fei, S. Lei, W.B. Zhang, W. Lu, Z. Lin, C.H. Lam, Y. Chai, Y. Wang, Direct TEM observations of growth mechanisms of two-dimensional MoS₂ flakes, Nat. Commun. 7 (2016) 12206, https://doi.org/10.1038/ncomms12206.